Highly Efficient Electron Stimulated Desorption of O^+ from Gadolinia-Doped Ceria Surfaces

Haiyan Chen,[†] Alex Aleksandrov,[†] Shaowu Zha,[‡] Meilin Liu,[‡] and Thomas M. Orlando*[,†]

School of Chemistry and Biochemistry and School of Materials Science & Engineering, Georgia Institute of Technology, Atlanta, Georgia 30332

Received: January 7, 2006; In Final Form: April 5, 2006

Highly efficient electron stimulated desorption of O^+ from gadolinia-doped ceria (GDC) surfaces annealed at 850 K in ultrahigh vacuum is observed and investigated. O^+ desorption has a major threshold of ∼40 eV and an intrinsic kinetic energy of ∼5.6 eV. Since the threshold energy is close to Ce 5s and Gd 5s core levels, Auger decay of core holes is likely associated with O^+ desorption from sites related to oxygen vacancies. The interactions of water and molecular oxygen with GDC surfaces result in a decrease in O^+ desorption, suggesting that water and oxygen molecules adsorb mainly to oxygen vacancies. The dependence of O^+ kinetic energies on the incident electron energy and temperature reveals surface charging as a result of electron trapping, hole trapping, and electron−hole recombination. The activation energy for surface charge dissipation is found to be 0.43 eV, close to the activation energy for ionic conduction (0.47 to 0.6 eV) in the same material.

I. Introduction

Ceria-based metal oxides have been widely studied as electrolyte and electrode materials for solid oxide fuel cells (SOFCs)[1−3] and as catalyst supports for many other applications. Among various doped ceria materials, gadolinia-doped ceria (GDC) is investigated as a promising electrolyte or a component of electrodes for lowering the operation temperature of SOFCs.[4−7,8−11] Similar to most mixed oxides, GDC has intrinsic oxygen vacancies. These vacancies play critical roles in the electrical conduction and chemical reactions occurring at the surfaces/interfaces of those electrode and electrolyte materials. In-depth understanding of the configuration and nature of different oxygen vacancies on the surfaces can further our understanding of the vacancy mediated or assisted surface processes, and thus enables us to achieve rational design of new materials for better fuel cell performance.

To date, various defects on the surface of several single crystal metal oxides have been directly characterized with scanning tunneling microcopy (STM)[12,13−16] and atomic force microscopy (AFM).[17−22] On the surface of CeO_2, for example, at least three types of surface oxygen vacancies or vacancy clusters have been observed by both techniques: isolated oxygen vacancies, linear surface oxygen vacancy clusters, and surface oxygen vacancy trimers. The relative population of each of these defects on the surface is determined by the densities of surface vacancies or the total number of oxygen ions removed from the surface. An atom-resolved noncontact atomic force microscopy (NC-AFM) study of $CeO_2(111)$[20] shows that the oxygen vacancy density on a nearly stoichiometric surface is in the range of $(0.8-1.7) \times 10^{12}$ cm^{-2}. Oxygen atom hopping was seen by NC-AFM at room temperature[19] but not observed by STM even at 300 to 400 °C.[14]

While both STM and AFM have been successfully used to characterize the surface defects on single crystal metal oxides, their application to polycrystalline mixed metal oxides has seen little success due to the complexity of the surface morphology. The defects on the surfaces of polycrystalline metal oxides may be studied by using probe molecules like molecular oxygen, which interact with the defects. Though the use of probe molecules has been very successful, this may alter the defects. The geometric relaxation or charge redistribution causes the oxygen ions directly coordinated to oxygen vacancies to have different chemical environments from other regular oxygen lattice ions. Probing these oxygen ions with appropriate techniques should generate information on surface defects, which often critically influence the surface catalytic properties of the oxides.

Electron stimulated desorption (ESD) is a surface specific technique that has been applied to the investigation of stimulated processes on metal oxide surfaces for decades.[23,24] Electron stimulated desorption of O^+ from metal oxide surfaces mainly comes from breaking the oxygen−metal bonds and therefore may bear important information regarding the oxygen ions adjacent to the oxygen vacancy sites. The properties and structures of these vacancies can therefore be extracted from carefully controlled O^+ ESD studies. Our past investigation of polycrystalline GDC surfaces using ESD has demonstrated a positive correlation of O^+ desorption yields and surface defect density.[25]

In this paper, we report highly efficient O^+ desorption from defect sites created by ultrahigh vacuum annealing. We examine the role of defects in the electron-stimulated desorption of O^+ from GDC surfaces annealed in ultrahigh vacuum. The interaction of these defects with H_2O and O_2 is also studied. Finally, the substrate temperature dependence of the O^+ kinetic energies is used to extract information on surface charge dissipation.

* To whom correspondence should be addressed. Phone: (+1) 404-894-4012. Fax: (+1) 404-894-7452. E-mail: thomas.orlando@chemistry.gatech.edu.

[†] School of Chemistry and Biochemistry.

[‡] School of Materials Science & Engineering.

10.1021/jp0601264 CCC: $33.50
Published on Web 05/16/2006

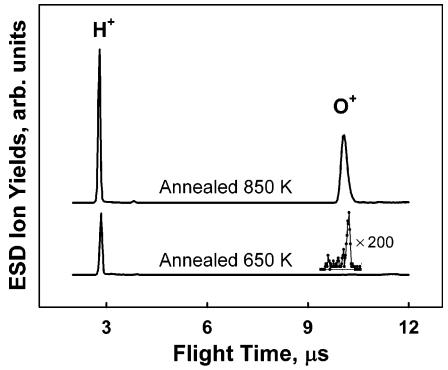

Figure 1. ESD-TOF spectra from GDC surfaces at room temperature. The GDC surfaces are annealed at 650 and 850 K. The incident electron energy is 200 eV and the pulse length is 200 ns. Note that the O^+ signal after annealing at 650 K is magnified 200 times.

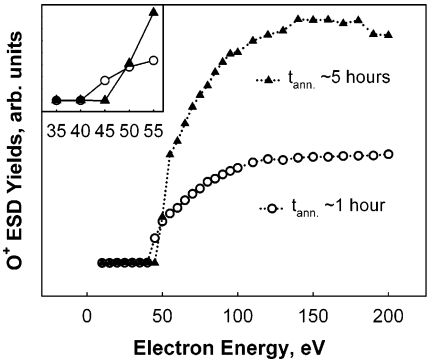

Figure 2. The energy dependence and annealing time dependence of O^+ ESD from GDC surfaces at room temperature. The annealing time ($t_{ann.}$) is ~1 h for the O^+ (○) data set and ~5 h for the O^+ (▲) data set. The inset shows the threshold region. The electron pulse length is 200 ns and the yields are normalized to the incident flux.

II. Experimental Section

The details of $Ce_{0.9}Gd_{0.1}O_{2-\delta}$ (GDC) sample preparation and characterization by X-ray diffraction and scanning electron microscopy were reported elsewhere.[25] The GDC samples used in this study have a polycrystalline fluorite structure (grain size 1 to 5 μm) and a significant number of grain boundaries. The dimensions of the GDC pellet were about $10 \times 6 \times 1$ mm^3.

ESD measurements were performed in an ultrahigh vacuum system with a base pressure of 2×10^{-10} Torr. The system is equipped with a quadrupole mass spectrometer, a time-of-flight (TOF) mass spectrometer, a pulsed low-energy electron gun, a calibrated dosing system, and a heating−cooling system.

The GDC sample was mounted to a conductive molybdenum plate that was used to heat the sample and to apply a bias. It was annealed to 400 °C to remove organic contaminants from the surface. The oxygen used is from Matheson with a purity of 99.998% and dosed into the chamber through a leak valve. Water was dosed to the surface through a directional doser after several freeze−pump−thaw cycles to remove dissolved gases. The sample was irradiated by the pulsed electron beam at 1000 Hz with an electron flux of 10^{14} electrons/(cm^2 s) during a given pulse or time-averaged currents of 200 pA to a few nA. Emitted cations were collected by applying a −50 V pulsed extraction potential to the TOF front lens assembly just after the end of the electron pulse. All ions were detected by using pulse counting with a transient digitizer. Three ESD-TOF spectra were taken at each electron energy and the average yield was used for threshold measurements. The yields were normalized to the electron beam current measured by a Faraday cup at each incident electron energy.

For ion kinetic energy measurements, both the extraction and tube potential were set to zero and the free field ion velocity distributions were measured. For each data point, at least five spectra were taken and averaged. A standard coefficient of deviation for the peak kinetic energy measurements was less than 1%. The Jacobian transform was used to calculate the ion kinetic energy distribution from the velocity distribution.

III. Results and Discussion

III.1. Highly Efficient O^+ ESD. TOF spectra of ions produced via pulsed electron irradiation of GDC surfaces at room temperature are presented in Figure 1. The incident electron energy was 200 eV and the samples were annealed at 850 and 650 K in vacuum. The main desorption products from both samples are H^+ and O^+. The H^+ yield from the sample annealed at 850 K is only 2.5 times that annealed at 650 K but the O^+ yield is more than 2 orders of magnitude greater. The enhancement of the O^+ ESD yield can be as high as 300 times with prolonged annealing time. This suggests that the surface sites for O^+ desorption on the GDC sample annealed at higher temperature are greatly different from those annealed at lower temperature, and the desorption mechanisms may also be different.

According to the NC-AFM study of defects on a $CeO_2(111)$[20] surface, the oxygen vacancy density increases with annealing time. The oxygen anion density on the top layer of $CeO_2(111)$ is 7×10^{14} cm^{-2}. Isolated oxygen vacancies are dominant when the vacancy density is below 1×10^{13} cm^{-2}. However, when the vacancy density is greater than 4×10^{13} cm^{-2}, vacancy clusters form. The vacancy density change is less than 50 times when comparing a surface with multiple defects to a nearly perfect surface. However, we observe an O^+ yield change of more than 2 orders of magnitude. The O^+ yield change then cannot be accounted for by the vacancy density change only. Line defects and triangular defects are likely present on the GDC surface annealed at 850 K and O^+ ESD from oxygen atoms associated with these types of defects is more efficient than that from isolated oxygen vacancies.

Shown in Figure 2 is the dependence of O^+ desorption on incident electron energy, which is very useful in elucidating the dominant desorption mechanisms. The O^+ ESD has a major threshold at 40 eV, with a very weak onset for O^+ around 20 eV. As seen in the inset, the major threshold shifts slightly to higher incident energy as annealing time increases.

Previous investigations on O^+ ESD from various metal oxides have demonstrated that O^+ desorption likely proceeds via an Auger-stimulated desorption mechanism described by the Knotek−Feibelman model.[26] On metal oxide surfaces, oxygen anions are considered to have a nominal negative charge of 2. To produce an O^+, three electrons need to be removed from the oxygen ion. According to the Knotek−Feibelman model, core holes of metal atoms are filled by electrons Auger cascading from the valence band formed primarily by the O 2p levels. This can produce multiple holes on terminal oxygen ions and can yield O^+. The Coulombic repulsion between the O^+ and neighboring metal ions desorbs nonthermal oxygen cations. This mechanism directly correlates desorption thresholds to the core level binding energies. For GDC, the 40 eV major threshold suggests that the desorption of O^+ originates from the core level excitation of Ce 5s (36.8 eV) and Gd 5s (46.2 eV), and the weak onset at 20 eV may be associated with the O 2s level (21.8 eV).[27−29] The peak O^+ kinetic energy is greater than 5.6

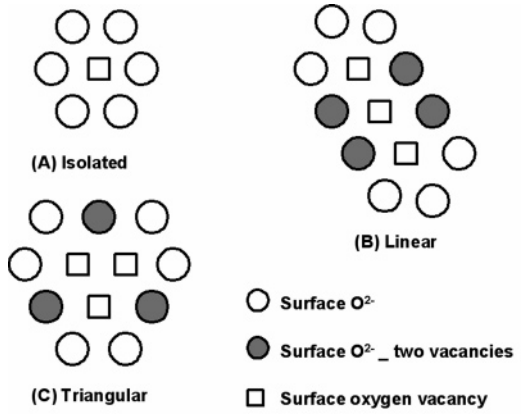

Figure 3. Structures of surface oxygen vacancies and vacancy clusters on a GDC(111) surface. Only the oxygen anions and vacancies in the top layer are shown.

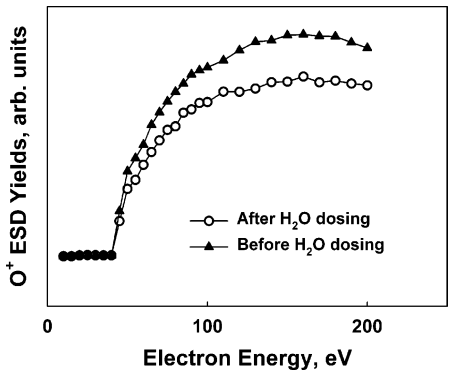

Figure 4. The energy dependence of electron stimulated desorption of O^+ from GDC surfaces before and after water dosing at room temperature. The pulse length of the electron beam is 200 ns. The base pressure of the chamber is 2×10^{-10} Torr and the water exposure is 100 L.

eV at room temperature (see section III.4), indicating that O^+ desorption is nonthermal. However, the above-mentioned three-electron interatomic Auger process is very inefficient as manifested by generally low O^+ ESD yields from metal oxide surfaces. This mechanism is therefore not enough to account for the extremely high O^+ yield observed from the polycrystalline GDC surfaces annealed at 850 K.

III.2. Electron Density on Oxygen Atoms and O^+ ESD. The charge on oxygen ions on the top layer of metal oxides is greatly influenced by their chemical environment, and in a mixed metal oxide it can be different from either of the oxide components. For example, first principle density functional calculations show that at least three different types of oxygen ions are present in $Ce_{0.8}Zr_{0.2}O_2$.[30] K-edge X-ray absorption near-edge spectroscopy supports that oxygen atoms in $Ce_{0.8}Zr_{0.2}O_2$ are in special chemical environments different from ZrO_2 or CeO_2. For $Ce_{0.8}Zr_{0.2}O_2$, the calculated Mulliken charge on oxygen ions is lower than that on ZrO_2 and CeO_2. For GDC, a mixed oxide similar to $Ce_{0.8}Zr_{0.2}O_2$, there may be surface defect sites with lower electron density on oxygen anions.

While the positive correlation between O^+ ESD yield and defect density on the GDC surfaces has been demonstrated,[25] it is observed at a grander scale in this experiment. A close examination of the influence of the neighboring oxygen vacancies on the charge of top layer oxygen atoms may provide insights into the desorption mechanisms. For oxygen vacancies, there are related defect states available in the band gap. If the defect state is empty, electrons from oxygen ions coordinated to the oxygen vacancy may delocalize to these defect states. As a result, the electron density on these oxygen atoms is lowered and the effective negative charge on each oxygen atom may appear <2.

Schematically illustrated in Figure 3 is the chemical environment of the top layer oxygen atoms adjacent to different types of vacancies on a GDC(111) surface. For oxygen ions coordinated to an isolated oxygen vacancy, the electrons on the oxygen have a chance to delocalize to one defect state. For oxygen atoms surrounding linear vacancy clusters and triangular clusters, one oxygen ion can be coordinated to two oxygen vacancies. Oxygen atoms surrounded by up to three vacancies can be seen on the STM image of $CeO_2(111)$.[14] Since there are more defect states available to the oxygen ions coordinated with vacancy clusters, the probability for electron transfer from oxygen to these defect states is high. This may even produce the equivalent of O neutral hopping on the surface. The O^+ desorption from this site should then be much easier than that from other sites since it is necessary to remove only one electron. As a matter of fact, we observe a very weak onset for O^+ desorption of $\sim$15 eV (data not shown), close to the first ionization potential of neutral oxygen atoms.

However, coordination to oxygen vacancies or vacancy clusters is not the only condition for highly efficient O^+ desorption. Under electron irradiation, the defect states of GDC trap electrons at lower electron energy and holes at higher electron energy.[31] If the defect states are filled, no electrons from oxygen atoms can be delocalized to the defect states. One pathway to lower the charge density from the defect states is via recombination of electrons with holes. This process is actually a charge neutralization process and may account for the shape of the O^+ ESD energy dependence curve and the influence of annealing history on threshold energies. The leading edge of the energy dependence curve is very steep, manifesting the underlying charge trapping and charge neutralization process. With increasing annealing time, more defects trap electrons, and more holes generated at higher incident energy are required to neutralize these electrons to lower the defect states occupancy. This is in agreement with the observed increase of negative charging and hence an increased threshold energy with annealing time.

III.3. Defect Healing by Water and Molecular Oxygen. From the above discussion, it is clear that the variation of surface defect density and occupation of defect states influences O^+ ESD. Water and molecular oxygen are known to adsorb to GDC surfaces dissociatively or nondissociatively at room temperature. These adsorption processes occur mainly at oxygen vacancy sites and therefore can either heal the defects or change the occupancy of defect states. In either case, the O^+ ESD yield is expected to be lower than that without adsorption.

At room temperature, the O^+ yield is decreased by $\sim$20% after GDC surfaces are exposed to $\sim$100 L of water, as seen in Figure 4. This O^+ yield decrease can be associated with the occupancy of oxygen vacancies by water molecules. The major threshold remains $\sim$40 eV, indicating that water adsorption does not change the primary Auger stimulated desorption channel. At the same time, the yield of H^+ ESD (not shown), an indicator of the amount of surface hydroxyl groups, is only slightly increased. These results suggest the concentration of preexisting surface hydroxyl groups does not change much and may indicate that the majority of water adsorption is nondissociative.

As shown in Figure 5, O_2 adsorption also decreases the O^+ ESD yield by $\sim$20%. This suggests that both water and oxygen adsorb to similar vacancy sites. A dynamic NC-AFM study

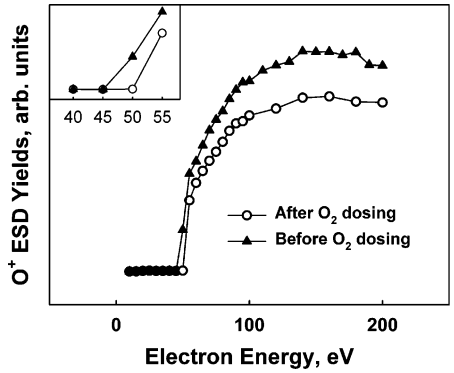

Figure 5. Electron energy dependence of O^+ ESD from GDC surfaces before and after molecular oxygen dosing. The pulse length of the electron beam is 200 ns. The base pressure of the chamber is 2×10^{-10} Torr and the oxygen exposure is about 100 L.

shows that molecular oxygen heals mainly the vacancy clusters instead of isolated vacancies.[20] Water may heal the same type of clusters, most likely linear vacancy clusters.

In contrast to water adsorption, the major O^+ ESD threshold shifts to higher electron energy after oxygen dosing. This is shown in the inset and a strong indication that oxygen adsorption can modify the occupancy of defect states. The higher threshold energy reveals that it is harder to remove the trapped electrons from defect states when O_2 is adsorbed. Since molecular oxygen has a positive electron affinity, O_2^- can form and be stabilized on the surface by electrostatic interactions with metal oxide surfaces. This can produce a Schottky barrier that traps electrons to the metal oxide surface and therefore decreases the number of empty defect states essential to effective O^+ desorption.

III.4. Dependence of O^+ Kinetic Energy on Incident Electron Energy and Temperature. A high-intensity O^+ ESD signal makes accurate kinetic energy measurements possible under various conditions. The kinetic energy of O^+ desorbed from the GDC surface is the sum of two components. One component originates from the Coulombic repulsion between desorbing O^+ and lattice cations and the other is from the acceleration by the electrical field induced by irradiation. For convenience of discussion, the former is referred to as the intrinsic kinetic energy, the latter as the surface potential, and the measured kinetic energy as the apparent kinetic energy. If the last step of nonthermal O^+ desorption is bond breaking and Coulombic repulsion, the intrinsic energy should not be influenced either by incident electron energy or surface temperature. Extrapolation of apparent kinetic energies should yield both the intrinsic kinetic energy as well as surface potentials for specific experimental conditions.

Presented in Figure 6 is the O^+ kinetic energy distribution obtained from pulsed 400 eV electron beam irradiation of GDC at room temperature. The kinetic energy range is from 5 to 15 eV, with a peak at 10.7 eV, two shoulders ~10 and ~7 eV, and a halfwidth of 3.7 eV. This halfwidth is comparable to the halfwidths of the O^+ kinetic energy distributions from the TiO_2-(110) surface[32,33] but narrower than that from the MgO(100) surface (>7 eV).[34] This O^+ kinetic energy distribution reveals that there are two or more types of O^+ desorption sites available.

Figure 7 represents the dependence of the O^+ peak kinetic energy on incident electron energy (E_i) at different temperatures. Clearly, measured peak O^+ kinetic energies increase with electron energy at all temperatures studied. For example, at room temperature, the peak O^+ kinetic energy at $E_i = 400$ eV is 10.7 eV whereas it is 5.6 eV at $E_i = 50$ eV. The increase of apparent kinetic energy with incident electron energy indicates that there

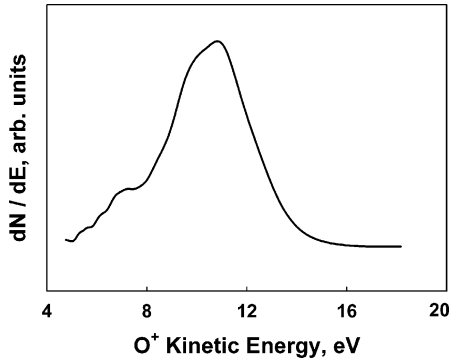

Figure 6. Apparent O^+ kinetic energy distribution obtained from pulsed (200 ns) 400 eV electron beam irradiation of the GDC surface at room temperature.

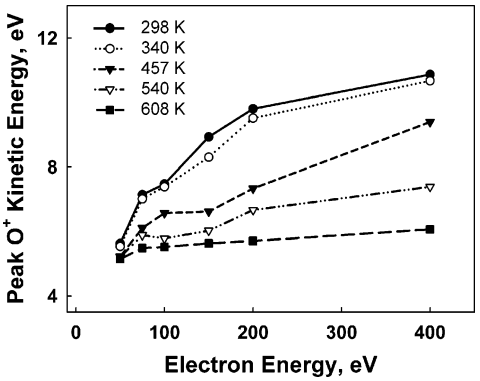

Figure 7. Energy dependence of the O^+ peak kinetic energy at different substrate temperatures.

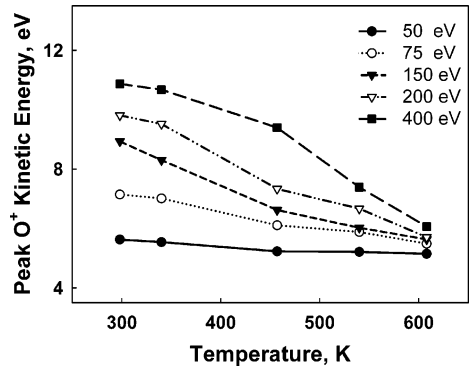

Figure 8. Substrate temperature dependence of O^+ peak kinetic energy at different incident electron energies.

is more positive charge on the surface at higher electron energy. Since negative surface charging at lower electron energy and charge neutralization has been observed on GDC, there might be a specific condition under which the surface is dynamically neutral and the apparent kinetic energy at this condition can be considered as the intrinsic kinetic energy. Interestingly, from Figure 7, the apparent kinetic energies appear to converge.

The influence of substrate temperature on the O^+ kinetic energy can be viewed more clearly in Figure 8. For all incident electron energies, the O^+ kinetic energies decrease with increasing temperature and tend to converge to the same energy at high temperature. The temperature influences the kinetic energy more sensitively at higher incident electron energy than at lower electron energies. Judging from the general trend of the influences of temperature and electron energy on O^+ kinetic energy, the intrinsic kinetic energy can be experimentally measured at low energy and high temperature. At 50 eV and 608 K, the peak O^+ kinetic energy is found to be 5.6 eV from

the average of many spectra. Water and oxygen adsorption have no influence on O^+ kinetic energy at room temperature. This result is well within the range of the reported O^+ kinetic energy from ESD of TiO_2(110) (4 and 7 eV)[33] and in agreement with the Coulombic repulsion from metal−oxygen bond breaking. With this measured intrinsic kinetic energy, the surface potential can be experimentally obtained by subtracting the intrinsic kinetic energy from apparent kinetic energy.

III.5. Surface Charge Dissipation. The surface potential is determined by the charge type and charge density on the surface. At higher electron energy, the dominant charge is positive. This can be an envelope of all positive charge carriers present on the surface, including holes trapped at Gd^{3+} sites or at lattice oxygen sites. If we assume the trapped positive charge on the surface forms a sheet of charge in an area of the electron beam spot size, then the charge density σ can be calculated from the surface potential. The charge density calculated from the surface potential determined this way is $\sim 1.2 \times 10^8$ e/cm^2 for a 400 eV electron beam at room temperature. This charge density is a measure of the difference between the charge produced at the surface and charge dissipated from the surface during the electron pulse, which has a pulse length of 200 ns. Therefore, the charge density on the surface can be treated as equivalent to the difference between the rate of charge production and charge dissipation. Since the charge generation is an electronic process that is determined by electron energy, then its rate can be considered as a constant C at fixed electron energy and independent of temperature. In contrast to charge production, the charge dissipation is a thermally activated process and is dependent on temperature. In general, the charge generation rate increases with electron energy and the hole dissipation rate increases with temperature. The measured peak O^+ kinetic energies represented by Figures 7 and 8 clearly display these trends.

During the pulse, the charge dissipation rate, $R_{\text{ch.d.}}$, defined as the number of charges dissipated from a unit area of the surface, is then proportional to the difference between the number of charges generated (constant at fixed electron energy) and the number of charges remaining on the surface (σ calculated from the surface potential), $R_{\text{ch.d.}} = C - \sigma$. An Arrhenius plot of this difference should yield a direct estimate of the activation energy for charge dissipation. Since at 400 eV the dominant surface charges are holes and the positive charge density is highest among all the measured energies, the 400 eV kinetic energy data are then chosen for an estimate of charge dissipation through GDC. The unknown constant is fitted with a minimum least-squares procedure and the result is presented in Figure 9. An apparent activation energy of 0.43 eV is found for the charge dissipation (R^2 value for the fit is 0.998).

Since the surface charge is positive, hole conduction is supposed to have significant contributions to the overall charge dissipation. However, for hole conduction through GDC, the activation energies extracted from electrochemical impedance measurements at very high oxygen partial pressure are very diverse. For example, the activation energies for p-type conductivity of $Ce_{0.8}Gd_{0.2}O_{2-x}$ were found to be 3.6,[35] 1.3,[36] and 1.5 eV[37] by different groups, and are much larger than 0.43 eV. This difference may suggest that hole migration may not be a dominant dissipation path. For GDC samples prepared with the same procedure as in this experiment, the activation energy for ionic conduction is between 0.47 eV[38] and 0.61 eV,[7] closer to 0.43 eV than that of hole conduction. It is therefore likely both electronic and ionic charge carriers are involved in surface charge dissipation. Since the nature of the charge carriers and the charge dissipation mechanisms are not clear, further investigation is warranted.

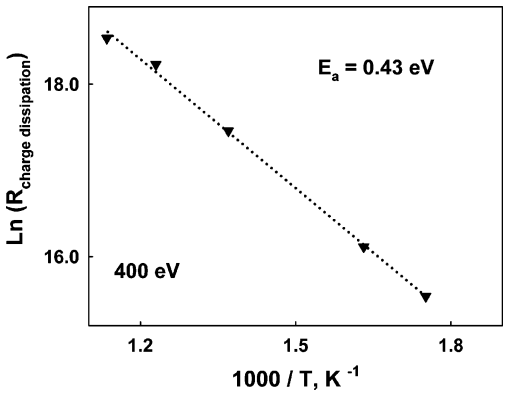

Figure 9. Arrhenius plot of the charge dissipation rate deducted from surface charge density. The incident electron energy is 400 eV and the pulse length is 200 ns.

IV. Conclusion

The investigation of highly efficient electron stimulated O^+ desorption from gadolinia-doped ceria surfaces annealed at 850 K in ultrahigh vacuum shows that O^+ ESD is mainly from the electronic excitation of Ce 5s and Gd 5s core levels. The high emission efficiency results from the increased overall density of oxygen vacancies, particularly the density of vacancy clusters. The chemical environment of oxygen ions and the occupancy of defect states can influence the electron density of oxygen anions and therefore the probability of O^+ desorption. Water and molecular oxygen interactions with GDC surfaces decrease the O^+ desorption yield, indicating that dissociative or nondissociative adsorption of these molecules occurs at vacancy sites. Surface potentials deduced from O^+ kinetic energy measurements performed at various incident electron energies and temperatures reveal surface charging. An apparent activation energy for charge dissipation is found to be 0.43 eV, not far from the activation energy for ionic conduction of GDC. In general, ESD can provide important information on the kinetics and dynamics of surface charging, charge transport, adsorption, and reactions occurring at defective insulating metal oxide materials.

Acknowledgment. This work was supported by the United States Department of Energy USDoE-NETL SECA Core Technology Program under Grant No. DE-FC26-02NT41572.

References and Notes

(1) Inaba, H.; Tagawa, H. *Solid State Ionics* **1996**, *83*, 1.
(2) Kharton, V. V.; Marques, F. M. B.; Atkinson, A. *Solid State Ionics* **2004**, *174*, 135.
(3) Park, S.; Gorte, R. J.; Vohs, J. M. *Appl. Catal., A* **2000**, *200*, 55.
(4) De Souza, S.; Visco, S. J.; De Jonghe, L. C. *J. Electrochem. Soc.* **1997**, *144*, L35.
(5) Gourba, E.; Briois, P.; Ringuede, A.; Cassir, M.; Billard, A. *J. Solid State Electrochem.* **2004**, *8*, 633.
(6) Marina, O. A.; Bagger, C.; Primdahl, S.; Mogensen, M. *Solid State Ionics* **1999**, *123*, 199.
(7) Xia, C. R.; Liu, M. L. *Solid State Ionics* **2002**, *152*, 423.
(8) Hart, N. T.; Brandon, N. P.; Day, M. J.; Lapena-Rey, N. *J. Power Sources* **2002**, *106*, 42.
(9) Leng, Y. J.; Chan, S. H.; Jiang, S. P.; Khor, K. A. *Solid State Ionics* **2004**, *170*, 9.
(10) Ralph, J. M.; Rossignol, C.; Kumar, R. *J. Electrochem. Soc.* **2003**, *150*, A1518.
(11) Tsoga, A.; Gupta, A.; Naoumidis, A.; Nikolopoulos, P. *Acta Mater.* **2000**, *48*, 4709.

(12) Norenberg, H.; Briggs, G. A. D. *Phys. Rev. Lett.* **1997**, *79*, 4222.
(13) Diebold, U. *Surf. Sci. Rep.* **2003**, *48*, 53.
(14) Esch, F.; Fabris, S.; Zhou, L.; Montini, T.; Africh, C.; Fornasiero, P.; Comelli, G.; Rosei, R. *Science* **2005**, *309*, 752.
(15) Norenberg, H.; Briggs, G. A. D. *Surf. Sci.* **1999**, *424*, L352.
(16) Norenberg, H.; Briggs, G. A. D. *Surf. Sci.* **1999**, *433*−*435*, 127.
(17) Bird, D. P. C.; de Castilho, C. M. C.; Lambert, R. M. *Surf. Sci.* **2000**, *449*, L221.
(18) Fukui, K.; Namai, Y.; Iwasawa, Y. *Appl. Surf. Sci.* **2002**, *188*, 252.
(19) Fukui, K.; Takakusagi, S.; Tero, R.; Aizawa, M.; Namai, Y.; Iwasawa, Y. *Phys. Chem. Chem. Phys.* **2003**, *5*, 5349.
(20) Namai, Y.; Fukui, K.; Iwasawa, Y. *J. Phys. Chem. B* **2003**, *107*, 11666.
(21) Namai, Y.; Fukui, K.; Iwasawa, Y. *Nanotechnology* **2004**, *15*, S49.
(22) Namai, Y.; Fukui, K. I.; Iwasawa, Y. *Catal. Today* **2003**, *85*, 79.
(23) de Segovia, J. L.; Williams, E. M. *Chem. Phys. Solid Surf.* **2001**, *9*, 608.
(24) Ramsier, R. D.; Yates, J. T., Jr. *Surf. Sci. Rep.* **1991**, *12*, 243.
(25) Chen, H.; Aleksandrov, A.; Chen, Y.; Zha, S.; Liu, M.; Orlando, T. M. *J. Phys. Chem. B* **2005**, *109*, 11257.
(26) Knotek, M. L.; Feibelman, P. J. *Phys. Rev. Lett.* **1978**, *40*, 964.
(27) Raiser, D.; Deville, J. P. *J. Electron Spectrosc. Relat. Phenom.* **1991**, *57*, 91.
(28) Teterin, Y. A.; Teterin, A. Y.; Lebedev, A. M.; Utkin, I. O. *Radiochemistry* (*Moscow, Russ. Fed.*) **1998**, *40*, 101.
(29) Teterin, Y. A.; Teterin, A. Y.; Lebedev, A. M.; Utkin, I. O. *J. Electron Spectrosc. Relat. Phenom.* **1998**, *88*−*91*, 275.
(30) Liu, G.; Rodriguez, J. A.; Hrbek, J.; Dvorak, J.; Peden, C. H. F. *J. Phys. Chem. B* **2001**, *105*, 7762.
(31) Chen, H.; Chen, Y.; Aleksandrov, A.; Dong, J.; Liu, M.; Orlando, T. M. *Appl. Surf. Sci.* **2005**, *243*, 166.
(32) Torquemada, M. C.; Desegovia, J. L.; Roman, E. *Surf. Sci.* **1995**, *337*, 31.
(33) Yakshinskiy, B.; Akbulut, M.; Madey, T. E. *Surf. Sci.* **1997**, *390*, 132.
(34) Colera, I.; Soria, E.; de Segovia, J. L.; Roman, E. L.; Gonzalez, R. *Vacuum* **1997**, *48*, 647.
(35) Costa, A. D. S.; Labrincha, J. A.; Marques, F. M. B. *J. Mater. Sci. Lett.* **1996**, *15*, 1716.
(36) Figueiredo, F. M.; Marques, F. M. B.; Frade, J. R. *J. Eur. Ceram. Soc.* **1999**, *19*, 807.
(37) Kharton, V. V.; Viskup, A. P.; Figueiredo, F. M.; Naumovich, E. N.; Yaremchenko, A. A.; Marques, F. M. B. *Electrochim. Acta* **2001**, *46*, 2879.
(38) Cheng, J. G.; Zha, S. W.; Huang, J.; Liu, X. Q.; Meng, G. Y. *Mater. Chem. Phys.* **2003**, *78*, 791.